


ORIGINAL ARTICLE

Open Access



Mechanism and Method of Testing Fracture Toughness and Impact Absorbed Energy of Ductile Metals by Spherical Indentation Tests

Jianxun Li¹, Tairui Zhang^{2*}, Shang Wang¹, Jirui Cheng¹ and Weiqiang Wang^{1,3*} 

Abstract

To address the problem of conventional approaches for mechanical property determination requiring destructive sampling, which may be unsuitable for in-service structures, the authors proposed a method for determining the quasi-static fracture toughness and impact absorbed energy of ductile metals from spherical indentation tests (SITs). The stress status and damage mechanism of SIT, mode I fracture, Charpy impact tests, and related tests were first investigated through finite element (FE) calculations and scanning electron microscopy (SEM) observations, respectively. It was found that the damage mechanism of SITs is different from that of mode I fractures, while mode I fractures and Charpy impact tests share the same damage mechanism. Considering the difference between SIT and mode I fractures, uniaxial tension and pure shear were introduced to correlate SIT with mode I fractures. Based on this, the widely used critical indentation energy (CIE) model for fracture toughness determination using SITs was modified. The quasi-static fracture toughness determined from the modified CIE model was used to evaluate the impact absorbed energy using the dynamic fracture toughness and energy for crack initiation. The effectiveness of the newly proposed method was verified through experiments on four types of steels: Q345R, SA508-3, 18MnMnNbR, and S30408.

Keywords Spherical indentation tests, Fracture toughness, CIE model, Impact absorbed energy

1 Introduction

Fracture toughness and impact absorbed energy are two crucial mechanical parameters that reflect a material's resistance to fracture. Accurate measurements of these two parameters are of great significance in evaluating the structural integrity of materials and ensuring equipment safety in long-term service. Conventional fracture tests and Charpy impact tests require destructive sampling, and thus cannot be used on in-service structures.

In contrast, the spherical indentation test (SIT), owing to its nondestructive and easy-to-perform nature, has been extensively investigated as a promising alternative to conventional destructive tests [1–5].

A method for estimating the quasi-static fracture toughness of materials from SITs was first proposed by Byun et al. [6], in which the work done by the average contact pressure in the direction of the impress was

*Correspondence:

Tairui Zhang
tairui_zhang@seu.edu.cn
Weiqiang Wang
sduefascf@163.com

¹ Key Laboratory of High-efficiency and Clean Mechanical Manufacture (Ministry of Education), National Demonstration Center for Experimental Mechanical Engineering Education (Shandong University), School of Mechanical Engineering, Shandong University, Jinan 250061, China

² School of Mechanical Engineering, Southeast University, Nanjing 211189, China

³ College of Electromechanical Engineering, Qingdao University of Science and Technology, Qingdao 266061, China

defined as the indentation energy necessary to fracture W_{IEF} . Then, the fracture toughness K_{IC} in $N/mm^{3/2}$ of the sample material can be determined by applying the Griffith theory [7]

$$W_{IEF} = \frac{1}{\pi a_C^2} \int_0^{h_C} P dh, \quad (1)$$

where h and h_C in mm are the indentation depth and critical indentation depth, respectively; a_C in mm is the critical contact radius (the contact radius a is the radius of the projection area of the indentation, and can be given as $(2Rh - h^2)^{0.5}$, where R is the radius of the indenter), and P in N is the external load ($P = Sh$, where S in N/mm is the slope of the loading line).

$$K_{IC} = \sqrt{2EW_F}, \quad (2)$$

where E is the Young's modulus of the specimen material. W_F in kJ/m^2 is the energy of formation for a unit area of a crack and can be approximated as W_{IEF} in kJ/m^2 .

To overcome the drawback of Byun's method, which requires an additional destructive tensile test, Haggag [8] empirically judged the critical indentation depth by considering the difference between brittle and ductile fractures (named Haggag toughness method, HTM). The calculation formula for fracture toughness was modified by considering the lower platform of the fracture toughness at low temperatures, as shown in Eq. (3):

$$K_{IC} = 30 + \sqrt{2EW_F}. \quad (3)$$

The HTM is applicable to a wide range of temperatures and does not require any additional destructive tests. However, the judgment of the critical indentation depth is empirical, and its effectiveness largely depends on the specimen materials [9]. Additionally, the HTM does not provide any explanation of the mechanism for obtaining the fracture toughness from SITs.

Using continuum damage mechanics (CDM), the mechanism of the fracture toughness calculation from SITs was investigated by Lee [10], who developed the critical indentation energy (CIE) model by finite element (FE) analysis and microscopic observation. The critical indentation energy is calculated as follows:

$$2W_f = \lim_{h \rightarrow h_C} \int_0^h \frac{P}{\pi a^2} dh, \quad (4)$$

where the term on the left represents the energy required for the formation of two crack surfaces. In Lee's definition, the value of W_f is only half of that defined by Haggag or Byun.

According to Griffith's theory, the fracture toughness K_{IC} can be calculated using Eqs. (4) and (2):

$$K_{IC} = \sqrt{\frac{ES}{\pi} \ln \left(\frac{2R}{2R - h_C} \right)}. \quad (5)$$

The CIE model, which introduced CDM to obtain the critical indentation depth, has been widely applied in previous studies [11–13]. However, the critical damage variable D^* used in the previous CIE model was determined from the analysis of a moving crack tip, in which the specimen was considered to be an elastic and perfectly plastic material (i.e., the hardening behavior was neglected) [14]. Additionally, the difference between the damage at high stress triaxiality and low stress triaxiality was neglected [15].

In contrast to numerous fracture toughness calculation models, few studies have evaluated the impact absorbed energy by SITs. The existing researches have primarily focused on correlating the impact absorbed energy to the quasi-static and dynamic fracture toughness [16]. Barsom et al. [17] conducted a large number of impact tests and conventional fracture tests, and proposed empirical formulae for the impact absorbed energy (KV_2), static fracture toughness (K_{IC}), and dynamic fracture toughness (K_{ID}). When J -integral theory was proposed, Hübner [18] established the relationship between fracture toughness and impact absorbed energy (J and KV_2) from the perspective of energy. Combining experimental and numerical approaches, Smith [19] contrasted the fracture behavior of pre-cracked fracture specimens tested quasi-statically with the Charpy V-notch specimens tested both quasi-statically and dynamically. They proposed an energy scaling model for relating the impact of the absorbed energy to the fracture toughness, which is suitable for both static and dynamic loading. Obtaining the impact absorbed energy from an empirical model is simple and reliable, but an empirical model often requires a large number of destructive tests for the determination of the fracture toughness, and these tests are more complex than impact tests.

To summarize, it can be seen from the aforementioned research that there are two or three methods for obtaining the fracture toughness of materials using SITs, but that the calculation accuracy of these models needs to be improved [20]. Studies on the fracture toughness and absorbed impact energy are relatively common. However, most testing methods require destructive sampling, which may not be suitable for in-service structures.

The authors of this study focused on proposing a method for determining the quasi-static fracture toughness and impact absorbed energy of ductile metals from SITs. The main technical route used in this

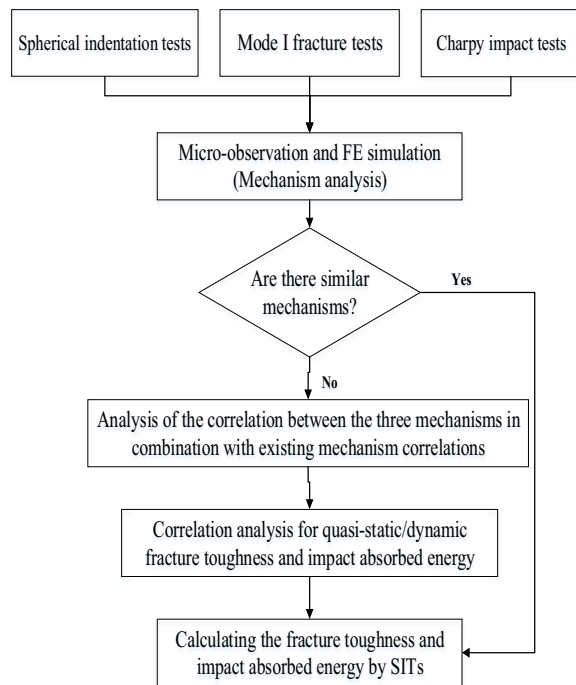


Figure 1 Main technical route

study is shown in Figure 1. The mechanism analysis for specimens under the SITs, mode I fracture tests, and Charpy impact tests were carried out with micro-observation and finite element (FE) calculations. The similarities of these damage mechanisms are discussed through comparison. Subsequently, based on the existing theory [21, 22] for mechanism correlation, a correlation analysis of the three damage mechanisms was conducted. Based on the correlation analysis of the quasi-static fracture toughness, dynamic fracture toughness, and energy for crack initiation, calculation methods for the fracture toughness and impact absorbed energy by SITs were proposed. Finally, the reliability of the proposed method was verified through experiments on four types of steel.

2 Experiments

2.1 Materials

Four types of steels commonly used for pressure vessels, Q345R, SA508-3, 18MnMoNbR, and S30408, were used in quasi-static tensile tests, dynamic tensile tests, mode I fracture tests, SITs, and Charpy impact tests. The chemical composition of each material was tested using the Bruker Tasman Q4 spectrograph and the results are provided in Table 1 with the corresponding standards.

Metallographic observations of Q345R, SA508-3, 18MnMoNbR, and S30408 are shown in Figure 2. It was found that the average grain size did not exceed 50 μm for all four metals, which indicates that the indenter can cover at least three grains even in the 1st cycle. Therefore, the effect of the indentation size was not considered.

2.2 Quasi-Static and Dynamic Tensile Tests

Quasi-static and dynamic tensile tests were conducted to obtain the tensile properties of the experimental materials under different strain rates. The quasi-static tensile specimens were machined into rod-shaped specimens with a diameter of 10 mm, a gauge length of 50 mm, and a total length of 194 mm in accordance with the Chinese standard [26]. The specific geometries of the tensile specimens are shown in Figure 3. Tensile tests were performed on an AG-IC universal testing machine at a loading speed of 1 mm/min until breakage, and the displacement was measured using an extensometer.

Dynamic tensile specimens were machined into plate specimens with a thickness of 3 mm, a gauge length of 40 mm, and a width of 12.5 mm in accordance with the Chinese standard [26]. A detailed configuration of the dynamic tensile specimens is shown in Figure 4. In accordance with the strain rate of the Charpy impact test (10 s⁻¹), strain-controlled (set tensile speed at 0.4 m/s) tests were conducted on HTM-5020.

In the high-strain-rate tests, the strain of a specimen was determined using digital image correlation (DIC) instead of the common extensometer measurements. Before the tests, speckles were sprayed onto the gauge

Table 1 Chemical composition of the material and corresponding standard values

Material	C	Si	Mn	Cr	Mo	Ni	Nb
Q345R	0.160	0.255	1.412	0.014	<0.001	0.0061	–
GB713–2014 [23]	≤0.20	≤0.55	1.20–1.60	≤0.30	≤0.08	≤0.30	–
SA508-3	0.226	0.194	1.475	0.956	0.469	0.227	–
ASME code [24]	≤0.25	0.15–0.40	1.20–1.50	0.40–1.00	0.45–0.60	≤0.25	–
18MnMoNbR	0.140	0.264	1.315	0.166	0.524	0.160	0.036
GB713–2014 [23]	≤0.21	0.15–0.50	1.20–1.60	≤0.30	0.45–0.55	≤0.30	0.025–0.05
S30408	0.048	0.479	1.170	18.33	0.049	8.248	0.0059
GB12771–2019 [25]	<0.08	≤0.75	≤2.00	18.00–20.00	–	8.00–11.00	–

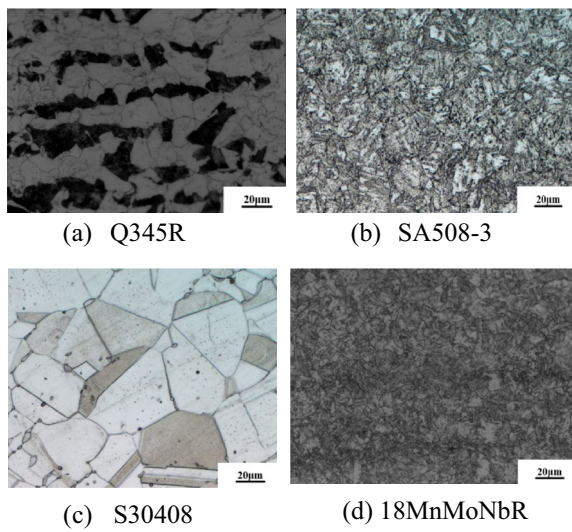


Figure 2 Metallography observation of Q345R, SA508-3, S30408 and 18MnMoNbR

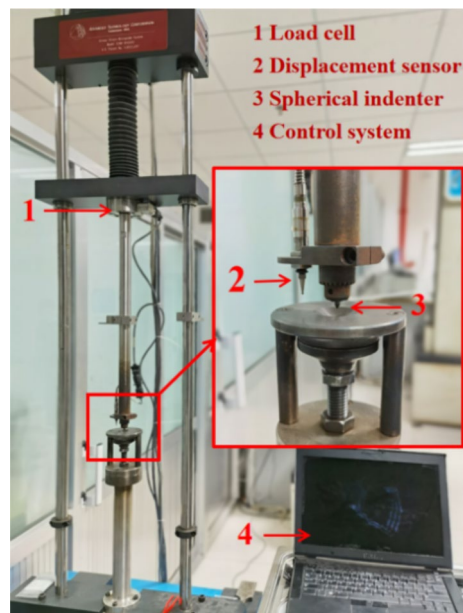


Figure 5 Stress-strain microprobe system B4000

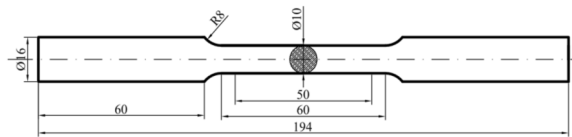


Figure 3 Configuration of the quasi-static tensile specimen (in mm)

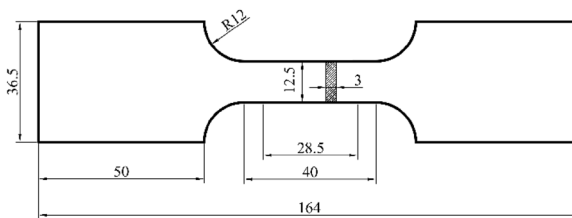


Figure 4 Configuration of the dynamic tensile specimen (in mm)

section of the specimens, and the speckle quality was calibrated statically. The speckle patterns in the tensile tests were captured using a super-high-speed digital camera (APX-RS) at a speed of 10^6 s^{-1} . Subsequently, the plastic strain distribution on the specimen surface was obtained using a commercial DIC system VIC-2D 6 (Correlated Solutions) and the captured images.

2.3 Spherical Indentation Tests

The specimens were cut into blocks with the dimensions $10 \times 10 \times 50 \text{ mm}^3$ and polished to a smooth surface. SITs were carried out on the stress-strain microprobe system B4000, as shown in Figure 5, using a tungsten carbide indenter with a diameter of 0.76 mm (Young's modulus

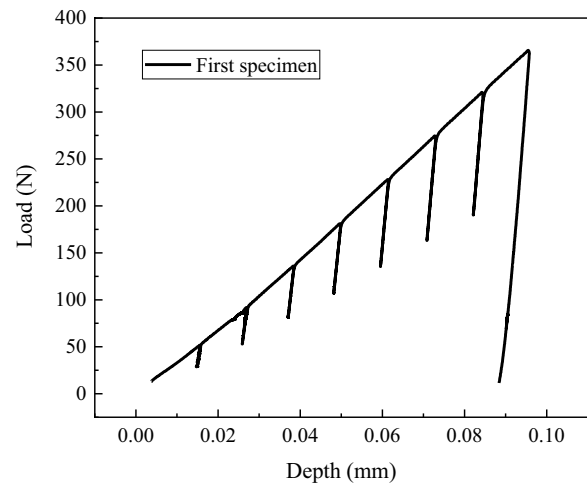


Figure 6 Load-depth curve from SITs

and Poisson's ratio of the indenter were 710 GPa and 0.23, respectively). Considering the quasi-static characteristics of the test, the loading and unloading rates were set to 0.1 mm/min. The load-depth curve obtained from the 8-cycle spherical indentation test is shown in Figure 6, whereby the maximum indentation depth h_{max} was set to $0.24R$.

2.4 Mode I Fracture Tests

Mode I fracture tests were conducted to determine the fracture toughness of the experimental materials. A

standard compact tensile (CT) specimen with a thickness of 0.45 inches and a ratio of nominal width to nominal thickness of 2 was used, as shown in Figure 7. Pre-cracking was performed on a high-frequency fatigue testing machine with the stress ratio and frequency set to 0.1 and 100 Hz, respectively. The fatigue crack length on the surface was recorded every 20000 cycles during pre-cracking while reversing the specimen to ensure that the crack lengths on both sides of the specimen were essentially the same. To strengthen the plane strain state of the fatigue crack tip, a side groove with a depth of 1.5 mm and an angle of 90° was machined onto the surface of the specimen after pre-cracking. CT tests were also performed on a stress-strain microprobe (SSM) system B4000.

Preformed cracks propagate slowly and steadily in ductile metals; thus, the plane strain fracture toughness K_{IC} cannot be ascertained directly. According to the relevant standard [27], the unloading compliance method can be used on a single specimen to determine the crack initiation resistance curve of ductile materials, that is, the J - R resistance curve. The intersection point of the structural line with a 0.2 mm offset and the J - R curve was used as the engineering fracture toughness, that is, J_{IC} in kJ/m^2 . Then, K_{IC} was calculated as

$$K_{IC} = \sqrt{\frac{E}{1 - \nu^2} J_{IC}} \tag{6}$$

2.5 Charpy Impact Tests

Charpy impact tests were conducted to obtain the crack initiation energy and the impact absorbed energy. The test was performed on an RKP450 impact testing machine with a hammer in accordance with the requirements of the Chinese standard [28]. To visually observe the processes of crack initiation and extension, the test was carried out on a self-designed tooling that stops the hammer after crack initiation and protects the sample from fracture. The configurations of the Charpy

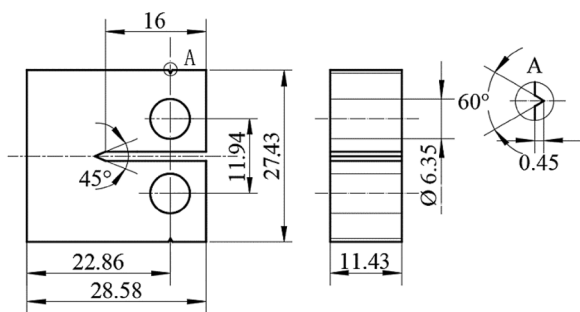


Figure 7 Configuration of the CT specimen (in mm)

impact test specimen and the tooling for crack arrest are shown in Figures 8 and 9, respectively. In Figure 9(a), the red box represents a cushion block, the green box represents the specimen, and the blue box represents the hammer. It has been reported that ductile metal materials crack when the hammer moves approximately 1.8 mm after impact along the end face of the specimen [29]. To ensure the effectiveness of the test, the crack arrest tests were carried out with cushion blocks of different thicknesses (11.7 mm, 11.8 mm, and 11.9 mm).

3 FE Simulation

Considering that the damage to ductile materials is closely related to their stress state, the SIT, mode I fracture, and Charpy impact tests were first numerically investigated using ABAQUS 6.14. The purpose of these simulations was to analyze the stress status of the specimens. Thus, a damage criterion was not developed in the calculations, and cracks were not allowed to propagate.

3.1 FE Modelling of Mode I Fracture Tests

Considering the characteristics of the CT specimen (mode I fracture), an FE model was developed. As a contrast to the SEM observations described in Section 4, the material properties of the specimens were characterized using a previously performed

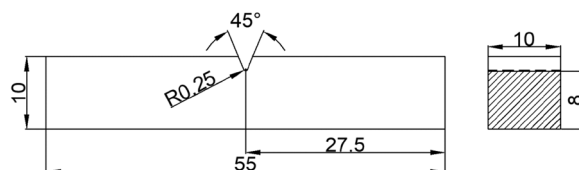


Figure 8 Configuration of the Charpy impact test specimen (in mm)

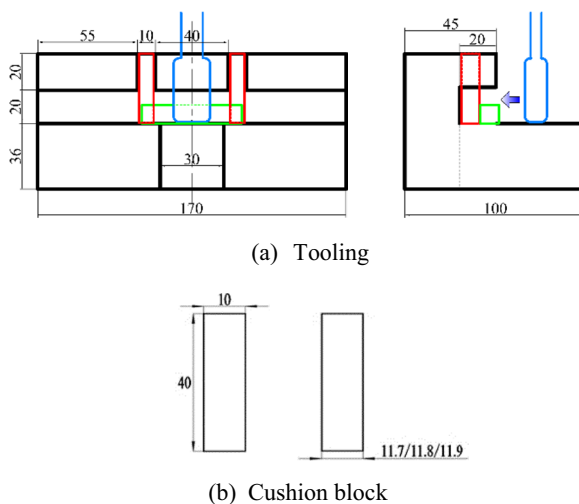


Figure 9 Configuration of the crack arrest tooling (in mm)

quasi-static tensile test on Q345R. In this calculation, the contact between the pin and the specimen was regarded as a surface-to-surface contact, with the friction coefficient set to 0.2 [30]. To ensure calculation accuracy and reduce cost, a 8-node linear brick with reduced integration (C3D8R in ABAQUS) was used. The meshes around the pre-cracked region (set to 2 mm × 2 mm) were gradually refined to 0.05 mm, while those in the distal region were set to around 0.4 mm, as shown in Figure 10. Similar to the fracture toughness test, the pin on the left of the model was fixed, and the pin on the other side was displacement-controlled with a maximum displacement of 3 mm.

A comparison of the load P -displacement q curve from the mode I fracture tests and the numerical simulations with different mesh densities is provided in Figure 11. The grid independence of the model was verified by refining the mesh size at the pre-crack tip to 0.15 mm, 0.10 mm and 0.05 mm. The initial part of the P - q curves from the FE calculations coincided well with the initial parts of those from the experiment. As the elastoplastic FE calculation did not consider the crack propagation in the CT specimen, the FE calculated P - q curves gradually deviated from their experimental counterparts after the crack began to propagate.

3.2 FE Modelling of Charpy Impact Tests

Considering the characteristics of the Charpy impact specimen, a quarter model, as shown in Figure 12, was created to determine the stress distribution and the variation in stress triaxiality σ_{Tri} at the V-notch tip. In this simulation, the Johnson-Cook model [31], shown in Eq. (7), was chosen for describing the mechanical

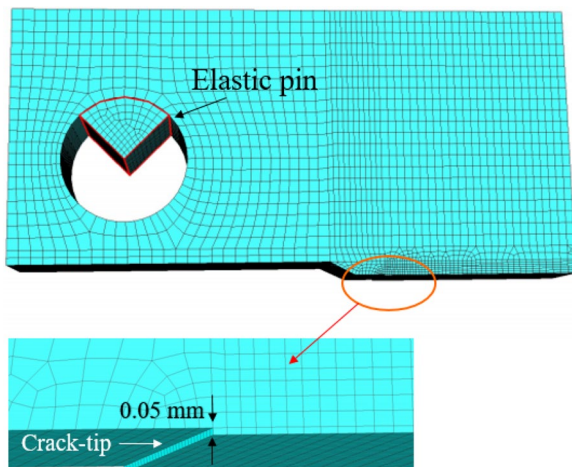


Figure 10 Illustration of the FE model of the mode I fracture tests

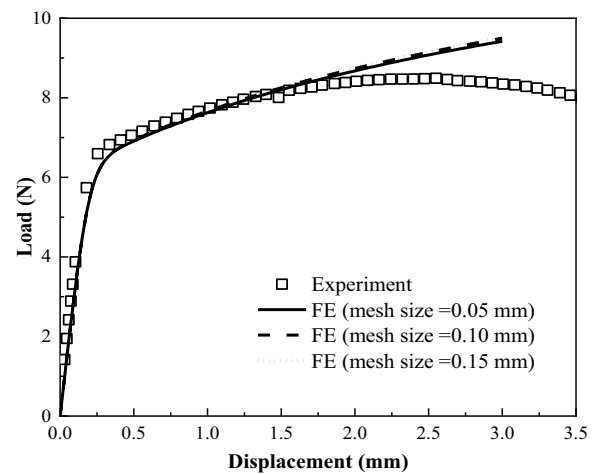


Figure 11 Comparison between P - q curves from FEA and CT test on Q345R

properties of the specimen (the temperature was not considered in this simulation).

$$\sigma_t = \left(A + B\varepsilon_p^n \right) \left[1 + C \ln \left(\frac{\dot{\varepsilon}_r^*}{\dot{\varepsilon}_r^*} \right) \right], \quad (7)$$

where σ_t is the flow stress, ε_p is the equivalent strain, $\dot{\varepsilon}_r^*$ represents the plastic strain rate, $\dot{\varepsilon}_r^*$ is usually taken as 1 s^{-1} and is the reference plastic strain rate. A , B , C , and n are material parameters that can be determined by fitting the data from the quasi-static and dynamic tensile tests of Q345R ($A = 332.53$, $B = 1015.68$, $C = 0.0128$, and $n = 0.56$).

8-node linear brick elements with reduced integration (C3D8R in ABAQUS) were used. The meshes around the V-notch and hammer tips were refined to 0.1 mm for calculation accuracy, and the overall mesh sizes of the specimens were 0.5 mm. According to the impact test, the initial velocity of the hammer was set to 5.2 m/s in the direction of the y -axis. The support was regarded as a rigid body, and its movement was fixed.

3.3 FE Modelling of SITs

Considering the characteristics of the SITs, an axisymmetric model was established for analyzing the

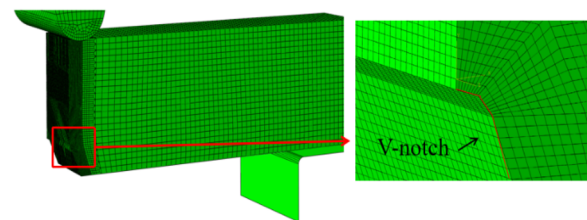


Figure 12 Illustration of the FE modeling of the impact test

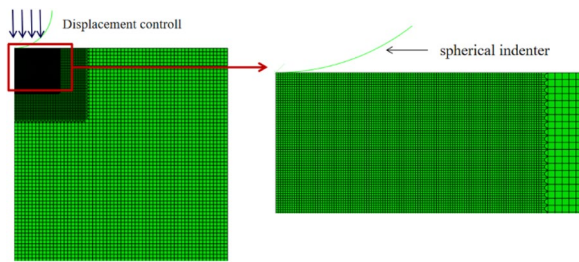


Figure 13 Illustration of the FE modeling of SITs

stress state, as shown in Figure 13. The indenter was considered as a rigid body whose diameter was the same as of that used in the experiment, while the mechanical properties of the specimen were determined by quasi-static tensile tests of Q345R.

The element type of the specimen was a 4-node bilinear axisymmetric quadrilateral with reduced integration (CAX4R). The contact settings of the SITs were similar to those in the FE model of the mode I fracture test, where the indenter and specimen surfaces were defined as the master and slave surfaces, respectively. According to a previous study [21], the minimum mesh size in the region near the indenter was 0.002 mm, and the maximum mesh size in the edge region was 0.018 mm. The FE calculation of the SIT involved displacement control, and the maximum depth was set in accordance with the SITs (i.e., $h_{max} = 0.24R$).

4 Calculation Method for Fracture Toughness Based on SITs

4.1 Stress State Analysis

4.1.1 Mode I Fracture Tests

The von Mises stress distribution of the pre-crack tip with a loading line displacement q of 1.5 mm (as the FE calculated P - q curves deviated from their experimental counterpart for $q > 1.5$ mm) on the specimen is shown in Figure 14(a). The maximum von Mises stress appears on the front edge of the pre-crack tip, and the stress concentration zone surrounding the crack has the shape of a pincer, which is the same as the theoretically determined plane strain plastic zone shape [7].

To better understand the stress state of the CT specimen, the stress triaxiality σ_{Tri} of the region before of the pre-crack tip, which was determined using Eq. (8), is shown in Figure 14(b):

$$\sigma_{Tri} = \frac{\sigma_m}{\sigma_{eq}}, \tag{8}$$

where σ_m and σ_{eq} are the hydrostatic and von Mises equivalent stresses, respectively. It can be observed that the stress triaxiality was relatively high near the bottom of the pre-crack in the specimen, which is regarded as a typical high stress triaxiality region ($\sigma_{Tri} \geq 0.4$). According to relevant studies [15, 32], failure of the high-stress triaxiality region is always caused by void nucleation, growth, and coalescence, which is called void accumulation fracture.

4.1.2 Spherical Indentation Tests

Similar to the spherical indentation tests, the simulation process consisted of eight times equal depth loading and unloading. The von Mises stress and shear stress

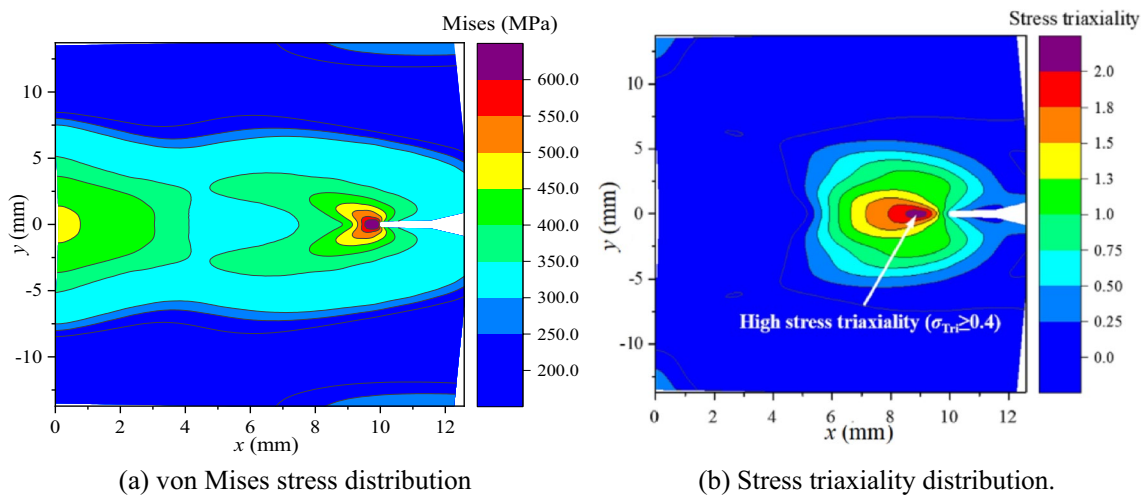


Figure 14 Mises stress and stress triaxiality distribution of CT specimen ($q = 1.5$ mm)

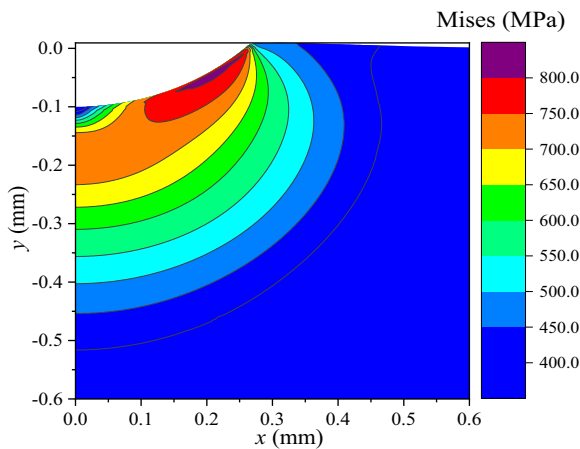


Figure 15 Mises stress distribution around indentation

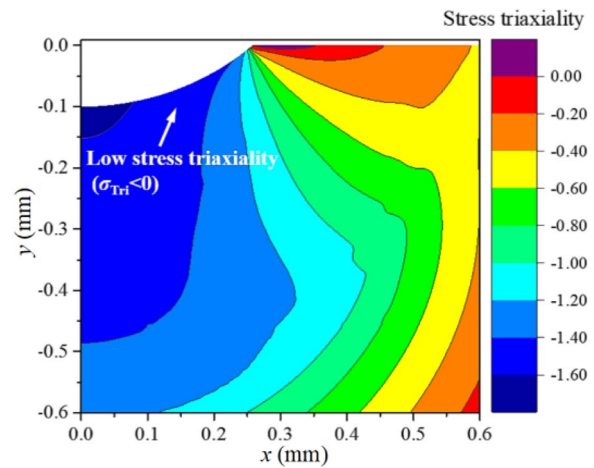


Figure 17 Stress triaxiality distribution around indentation

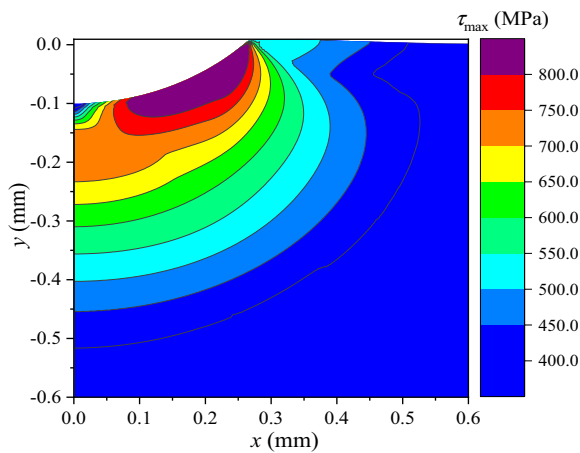


Figure 16 Shear stress distribution around indentation

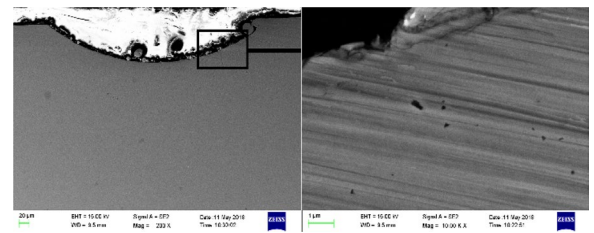


Figure 18 Microstructure of residual indentation

distributions at the end of the 8th loading ($h=0.24R$) around the indentation area are presented in Figures 15 and 16, respectively. It can be seen that the distributions of the von Mises stress and the shear stress are basically the same and approximately in the shape of a spherical crown, where the maximum values are located in the 45° – 60° range inclined to the y -axis. Owing to friction, the plastic flow at the indentation bottom was suppressed, leading to a relatively small stress at the indentation center.

The stress triaxiality σ_{Tri} in the area around the indentation, as shown in Figure 17, is almost entirely negative. The minimum stress triaxiality was less than -1.6 at the bottom of the indentation, while the maximum was located at the edge of the indentation with -0.2 . This indicates that the region around the indentation is a typical low-stress triaxiality region

($\sigma_{Tri} \leq 0$), where the fracture always occurs due to shear stress-induced damage [15, 32].

4.2 Damage Mechanism Analysis

All microscopic observations were performed using the same material (Q345R) to ensure consistency. The micromorphology of the indentation section surface is shown in Figure 18, in which several wedge-shaped voids are visible around the border of the residual indentation. This is similar to the shear damage explained by dislocation pile-up [33]. It was found that many wedge-shaped voids are located in the ‘wing region’ (i.e., the 45° – 60° range inclined to the y -axis), while almost no voids were observed at the indentation bottom. The damage distribution is consistent with the shear stress concentration presented in Section 4.1.2. Thus, it can be concluded that shear stress is the main reason for the initiation and localized distribution of voids in the indentation test, and that the damage mechanism in SITs is the same as that in the pure shear test. As reported in a previous study [21], the mode I fracture surface exhibits a typical dimple feature, which is similar to the tensile fracture. The micromorphology near the crack tip is shown in Figure 19, with several spherical or ellipsoidal voids visible in the region under mode I loading.

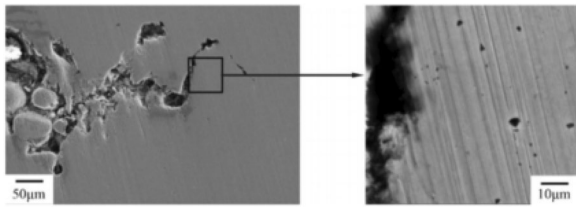
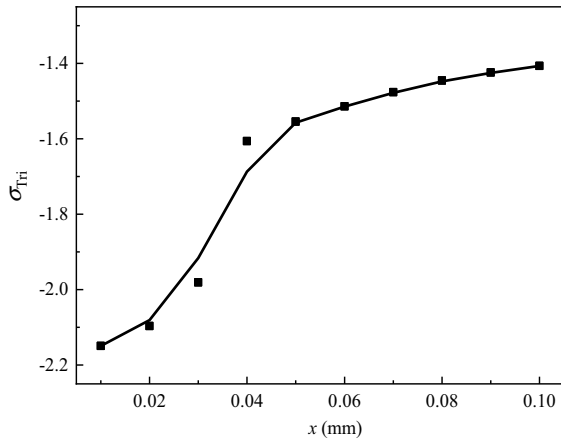
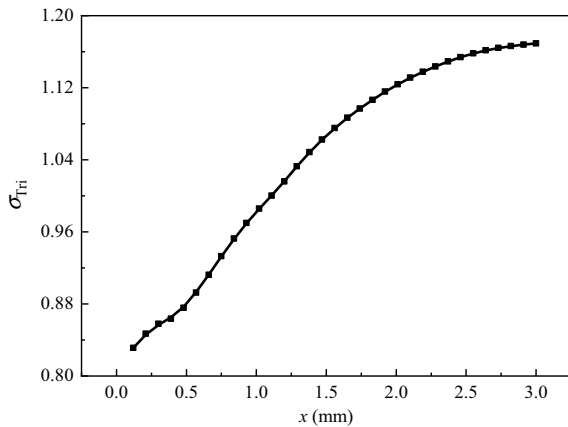


Figure 19 Observation of section surface for mode I specimen [21]



(a) Variation in σ_{Tri} with h in region of maximum shear stress.



(b) Variation in σ_{Tri} with q at crack tip under mode I loading.

Figure 20 Comparison of σ_{Tri} from FE calculations on SITs and the mode I fracture at damage zone

To analyze the relationship between the fracture mode and the stress status, a comparison of the stress triaxiality-load deflection curves at the stress concentration zone in the FE model of SITs and the mode I fracture (which corresponds to the damage concentration area in microscopic observations) is

provided in Figure 20. σ_{Tri} increased significantly with h at the beginning of loading, but finally stabilized at approximately -1.4 . Combined with the microstructure of the residual indentation, it was proved that the inner damage of the material was caused by shear stress, and that the material more easily produced shear failure in the low stress triaxiality region. As shown in Figure 20(b), σ_{Tri} varies between 0.8 and 1.2, indicating that the damage in the mode I specimen is similar to that in the uniaxial tensile tests, originating from the nucleation, growth, and coalescence of voids in the high-stress triaxiality region [15, 32].

The mechanisms of tensile and shear fractures are essentially different. However, the initiation and growth of voids and microcracks lead to a decrease in the effective bearing area, and thus, cause a reduction in the effective elastic modulus (Young’s modulus is used to characterize tensile damage, and the shear modulus is used to characterize shear damage). According to continuum damage mechanics, the tensile damage variable D_I and the shear damage variable D_{II} can be determined using Eqs. (9) and (10), respectively [34]:

$$D_I = 1 - \frac{E_{eff}}{E}, \tag{9}$$

$$D_{II} = 1 - \frac{G_{eff}}{G}, \tag{10}$$

where E_{eff} , G_{eff} and G are the effective Young’s, effective shear, and shear moduli of the undamaged material, respectively.

Shi et al. [22] proposed a critical damage strain energy release rate Y^* , as shown in Eqs. (11) and (12), for the tensile and shear forces, respectively is a material constant that is independent of the stress state (i.e., $Y_I^* = Y_{II}^*$):

$$Y_I^* = \frac{\sigma_C^2}{E(1 - D_I^*)}, \tag{11}$$

$$Y_{II}^* = \frac{(1 + \nu)\tau_C^2}{E(1 - D_{II}^*)}, \tag{12}$$

where ν is Poisson’s ratio and can be considered as a material constant for each type of metal (e.g., 0.3 for steels used in this study). D_I^* is the critical tensile damage variable and D_{II}^* is the critical shear damage variable of the material.

According to von Mises yield criterion, there is:

$$\sigma_C = \sqrt{3}\tau_C, \tag{13}$$

substituting Eq. (11), and Eq. (12), into Eq. (13), yields Eq. (14):

$$\frac{1 - D_I^*}{1 - D_{II}^*} = \sqrt{\frac{3}{2(1 + \nu)}}. \tag{14}$$

According to a mechanism analysis, the critical damage variables under the mode I fracture test and the SITs correspond to D_I^* and D_{II}^* , respectively.

4.3 Modified CIE Model

The previous CIE model creatively introduced CDM into the indentation test, but the model has some shortcomings, as mentioned in Section 1. First, the critical damage variable D^* used in the previous CIE model was derived from Andersson’s numerical analysis [35], in which the object was assumed to be an elastic perfectly plastic material (i.e., the effect of work hardening was neglected). In addition, D^* has not yet been experimentally verified. Moreover, the difference between the damage mechanisms in high stress triaxiality and low stress triaxiality regions was neglected in the model.

To obtain the critical damage variable of the materials, cyclic loading tensile tests were performed, as mentioned in Section 2.2. The true stress-strain curve of Q345R is shown in Figure 21. Considering the effect of necking on the determination of the stress-strain curve, only the data before obvious necking were used. In addition, only the first 40% of the unloading curve data were used to avoid the effect of back-stress relaxation [36].

The variation in D_I with the true strain is shown in Figure 22. The damage variable of the four materials initially increased with an increase in the true strain and

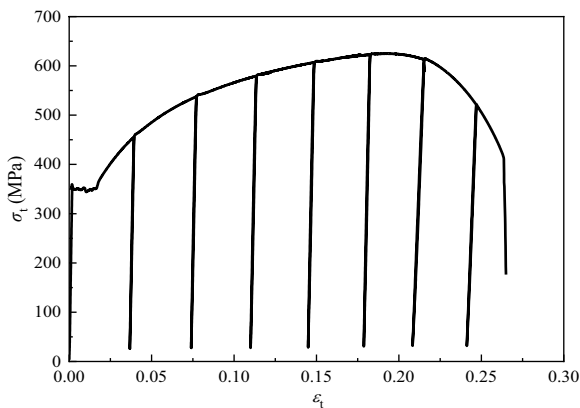


Figure 21 True stress-strain curve from cyclic loading tensile tests (Q345R)

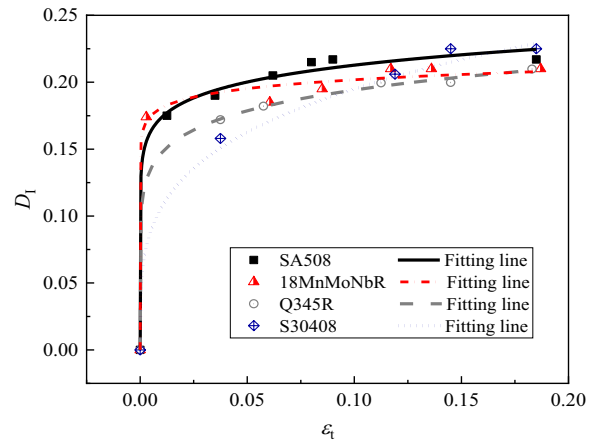


Figure 22 Variation in tensile damage with true strain

then tended to remain constant. As shown in Figure 22, the value of the critical damage variable D_I^* ranged between 0.20 and 0.23, which is consistent with D_I^* (approximately 0.22) as measured through tension tests by predecessors [34]. To obtain a more conservative fracture toughness calculation for engineering applications, a conservative value of $D_I^* = 0.2$, was used for all materials in this study. According to Eq. (14), the critical shear damage variable of all materials, D_{II}^* was calculated to be 0.25. Because the damage around the indentation was almost entirely caused by shear stress, the critical indentation depth h_c should be determined by D_{II}^* .

To determine E_{eff} from SITs, the Pharr-Oliver formula was used in the previous CIE model [37]. However, it is important to note that the plastic deformation of the specimen before unloading was not considered in the Pharr-Oliver formula, that is, Eq. (15), which leads to an evident reduction in the effective Young’s modulus at a small indentation depth [37, 38]:

$$E_{PO} = \frac{1 - \nu^2}{2a/L - (1 - \nu_{ind}^2)/E_{ind}}, \tag{15}$$

where ν and ν_{ind} are the Poisson’s ratios of the specimen and spherical indenter, respectively; L in N/mm is the slope of the unloading curve in the load-displacement curve obtained from the SITs, and E_{ind} is the Young’s modulus of the spherical indenter.

To consider the plastic deformation of the material during SITs, a modified effective Young’s modulus formula was proposed in our previous study [30], as follows:

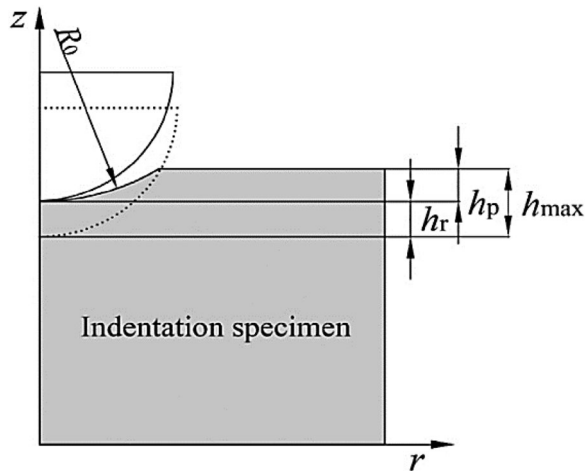


Figure 23 Illustration of the residual indentation surface [10]

$$E_{eff} = \frac{1 - \nu^2}{2\sqrt{\frac{h_r R_0}{R_0 - R}} / L - (1 - \nu_{ind}^2) / E_{ind}}, \quad (16)$$

R_0 and h_r in mm are the radius of the residual indentation and secondary loading depth, respectively, and are obtained using Eqs. (17) and (18), respectively:

$$R_0 = \frac{h_p^2 + (2h_{max}R - h_{max}^2)}{2h_p}, \quad (17)$$

$$h_r = h - h_p, \quad (18)$$

where h_{max} and h_p are the maximum and residual indentation depths, respectively, as shown in Figure 23.

It was found from experiments that the relationship between $\ln E_{eff}$ and $\ln h$ can be described by a linear function, as shown in Figure 24.

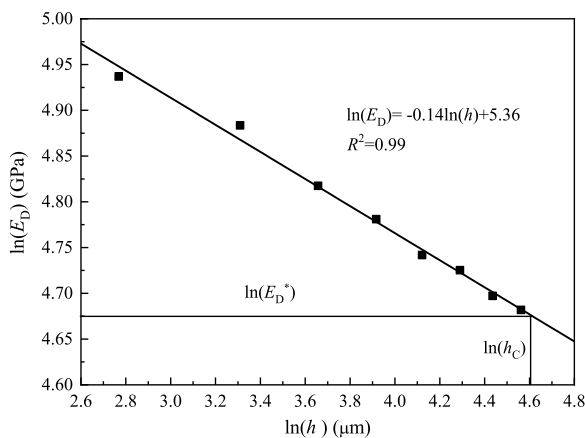
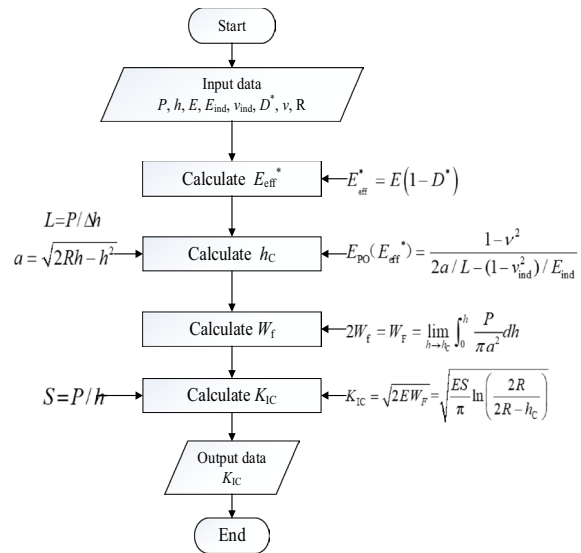
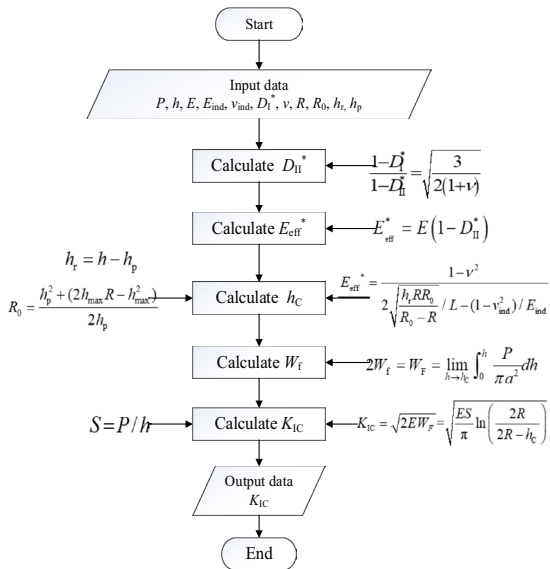


Figure 24 Linear correlation between $\ln E_{eff}$ and $\ln h$ (SA508-3)



(a) Previous CIE model



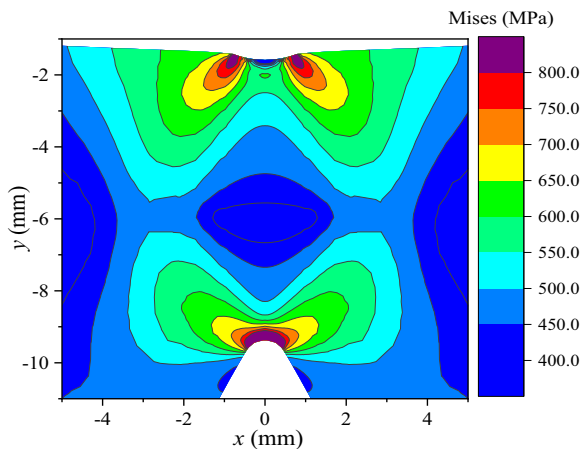
(b) Modified CIE model

Figure 25 Calculation process of fracture toughness

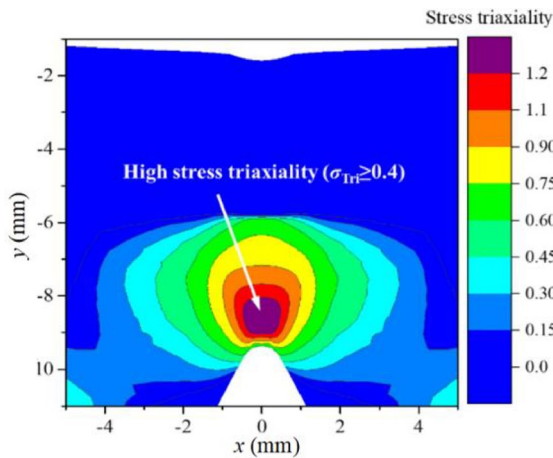
Similar to the previous CIE model, the critical effective Young's modulus E_{eff}^* can be calculated using Eq. (19), where D_{II}^* and E are known:

$$E_{eff}^* = E(1 - D_{II}^*). \quad (19)$$

The critical indentation depth h_c can then be determined using the fitting curve shown in Figure 24. The fracture toughness can be calculated using Eq. (5), with h_c . An illustration of the calculation processes of the previous and modified CIE models is shown in



(a) von Mises stress distribution



(b) Stress triaxiality distribution.

Figure 26 Mises stress and stress triaxiality distribution of specimen under impact test

Figure 25(a) and (b), respectively. The variation in the effective Young’s modulus was used in both models for determining the h_C , which was used to calculate W_F and then K_{IC} , while the modified model was used in the calculation of E_{eff} and the judgement of the critical damage.

5 Calculation Method of Impact Absorbed Energy Based on SITs

5.1 Stress State Analysis of Impact Test

According to the displacement and the drop speed of the hammer during the crack arrest test, the Mises stress and the stress triaxiality distribution of the impact specimen when h reached 1.8 mm (initiation of crack propagation) are shown in Figure 26. The stress concentration zone can be seen in the vicinity of the V-notch, which is in

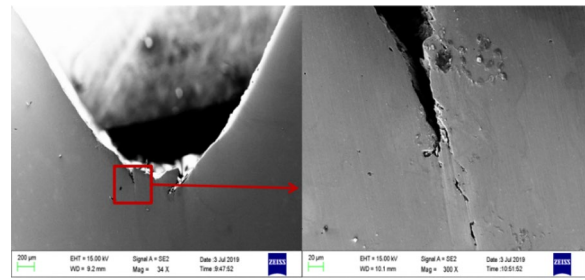


Figure 27 SEM observation of section surface for crack arrest specimen (Q345R)

the shape of a bowknot. The stress gradually decreased from the middle to both sides, with the maximum located at 1 mm in front of the bottom of the V-notch. From Figure 26(b), it was found that the stress triaxiality around the stress concentration zone was greater than 0.4, which is regarded as a typical high-stress triaxiality region, indicating that the main factors resulting in damage to the specimen were void nucleation, growth, and coalescence [15, 32].

5.2 Damage Mechanism Analysis

The SEM observations of the section surfaces of the crack-arrest specimens are shown in Figure 27. Voids and microcracks can be observed in front of the crack tip, which is located in the high-stress triaxiality region mentioned in the numerical analysis. According to micro-mechanics, the initiation of voids can be explained by the fact that the local stress in the damage region could effectively offset the bonding force between the particles and the matrix. Moreover, the volume of voids increases rapidly, particularly in the high-stress triaxiality region. With the development of voids, adjacent voids coalesce, leading to the initiation and propagation of microcracks. This damage morphology was similar to that of the CT specimen, as shown in Figure 19. An observation of the fracture surface of the impact test specimen (Q345R), shown in Figure 28, shows obvious dimple features,

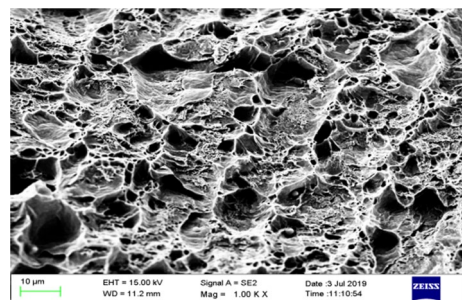


Figure 28 SEM observation of fracture surface for impact test specimen (Q345R)

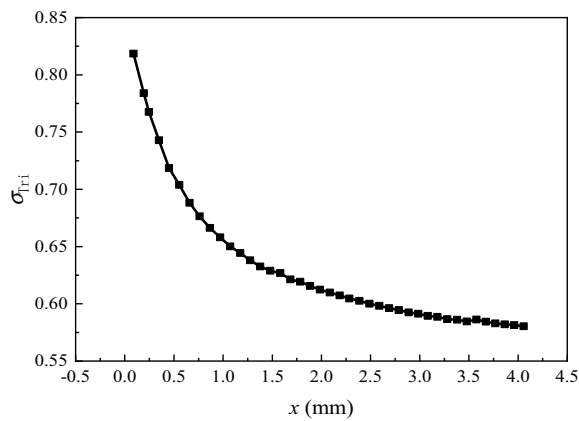


Figure 29 Variation of σ_{Tri} with displacement of hammer x (region of crack tip)

which are similar to those of the CT specimen [21]. The variation in σ_{Tri} with the displacement of the hammer, shown in Figure 29, also proved the impact damage formed in the high stress triaxiality region, similar to the CT specimen shown in Figure 20(b). Therefore, it can

be concluded that the impact specimen shares the same tensile damage mechanism with the CT specimen.

5.3 Correlation between Dynamic and Quasi-Static Fracture Toughness

High strain rate loading affects the yield strength of the specimens, which is known as the strain rate effect. Therefore, the variation in yield strength can reflect the strain rate effect of the materials to a certain extent. Based on this, Chaouadi et al. [39] proposed a method for characterizing the relationship between the dynamic and quasi-static fracture toughness (J_{IC} to J_{ID}) using yield strength:

$$\frac{J_{IC}}{J_{ID}} \approx \alpha \left(\frac{\sigma_{YD}}{\sigma_{YS}} \right)^2, \tag{20}$$

where σ_{YD} in MPa is the dynamic yield strength, σ_{YS} in MPa is the quasi-static yield strength, and α is the proportion coefficient.

This method was verified by Pan et al. [16] through a large number of experiments on Q345R, from which the constant α was determined as being 0.28 (with a

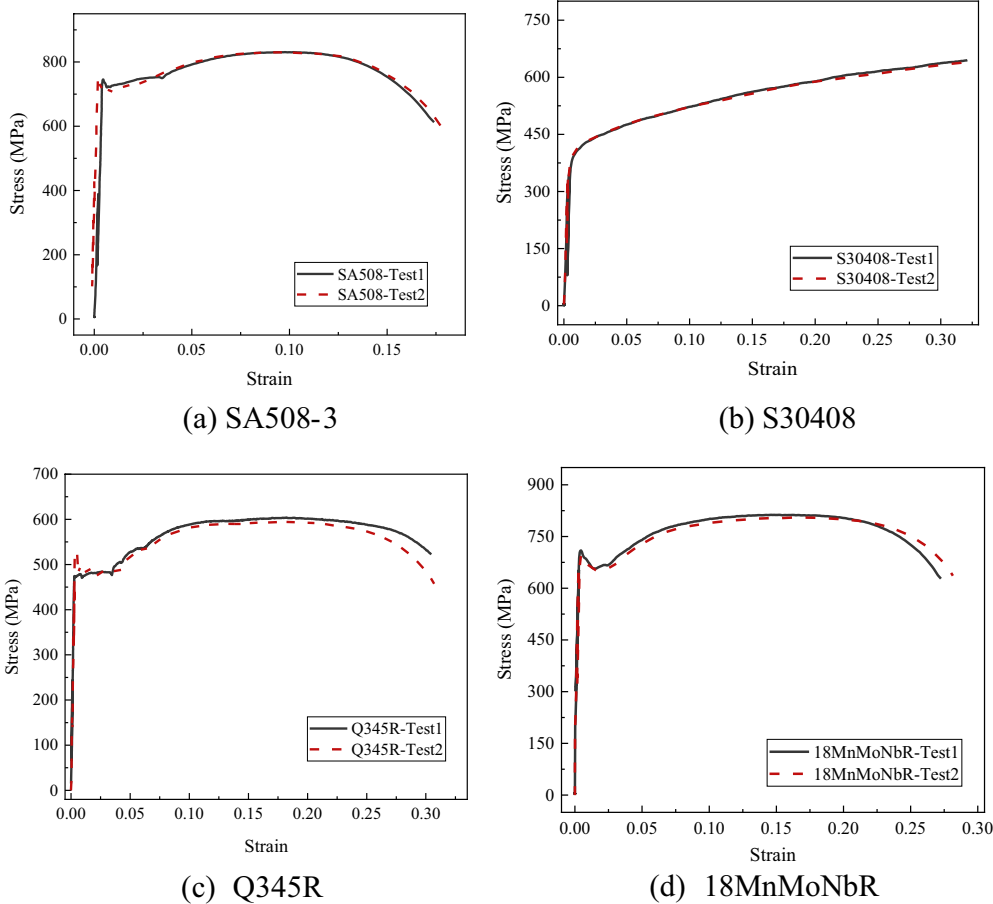


Figure 30 Stress-strain curves under dynamic tensile testing with tensile speed of 0.4 m/s

Table 2 Dynamic and static yield strengths of each material

Material	σ_{YD} (MPa)	σ_{YS} (MPa)	σ_{YD}/σ_{YS}
SA508-3	714	560	1.275
18MnMoNbR	843.2	680	1.24
S30408	362	278	1.30
Q345R	475	373	1.273
Average value			1.258

ratio of J_{IC} to J_{ID} of 0.44 determined from quasi-static and dynamic J - R curves). The engineering stress-strain curves from the dynamic tensile tests mentioned in Section 2 are presented in Figure 30, with the corresponding yield strengths shown in Table 2. The average ratio of σ_{YD} to σ_{YS} was 1.258. Compared with the ratio in Ref. [34], the ratio of J_{IC} to J_{ID} determined from the tests in this study was 0.443 (the difference was less than 1%).

5.4 Correlation between Dynamic Fracture Toughness and Impact Absorbed Energy

Due to the complexity of dynamic fractures, the solution of most problems still has to be based on numerical analysis or empirical formulae, with a few exceptions, such as an infinite crack body and a plane crack in elastic-perfectly plastic material. However, the finite element method cannot be used to obtain the dynamic fracture parameters of a material. Therefore, the empirical correlation method is currently the main approach for analyzing dynamic parameters [40, 41].

Based on the impact tests conducted by Chaouadi [29], the location of crack initiation can be determined from the load-displacement curve. As shown in Figure 31, crack initiation occurred at a load between the general yield (i.e., F_{gy}) and the maximum load (i.e., F_{max}). The initiation load can be written as

$$F_{init} \approx \frac{F_{gy} + F_{max}}{2} \tag{21}$$

The impact absorbed energy KV_2 is the area under the load-displacement curve, which can be obtained by integrating over the entire curve. The energy-to-crack initiation KV_{2i} is the area of the purple zone, which can also be determined by the curvilinear integral.

The experimental data were analyzed from the viewpoint of energy, and it was found that the ratio of KV_{2i} to KV_2 is η , which is approximately equal to a constant, as shown in Eq. (22):

$$KV_2 = KV_{2i} / \eta \tag{22}$$

The Charpy impact tests shown in Section 2.5 yield an η of around 7%, which coincided well with those provided in previous studies [16, 29]. Thus, the authors attempted to determine the relationship between the dynamic fracture toughness J_{ID} and the impact absorbed energy KV_2 by correlating J_{ID} and KV_{2i} . The specific analysis is as follows.

Comparing the damage mechanisms mentioned in Sections 4.2 and 5.2, it was concluded that the V-notch tip of the impact specimen and the crack tip of the mode I fracture specimen were observed in the high stress triaxiality region. Furthermore, they shared the same fracture mechanism, in which the damage was caused by the nucleation, growth, and coalescence of voids under tensile stress fields. Therefore, the Charpy impact test can be correlated with the mode I fracture test, which helps to prove that there is a certain quantitative relationship between the dynamic fracture toughness and the crack initiation energy, and also explains that it is rational to calculate the impact absorbed energy by SITs.

As shown in Table 3, the quasi-static fracture toughness J_{IC} was obtained by the mode I fracture test, and J_{ID} was calculated using Eq. (20). The crack initiation energy was determined using the load-displacement curve from

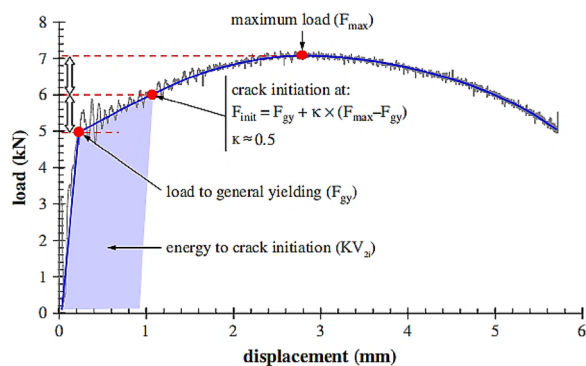


Figure 31 Determination of the onset of crack initiation using the load-displacement curve [29]

Table 3 Fracture toughness and impact crack initiation energy from tests

Material	No.	J_{IC} (N/mm)	J_{ID} (N/mm)	KV_{2i} (J)
S30408	1	118.60	269.55	21.76
	2	120.10	272.95	22.05
SA508-3	1	146.07	331.98	16.19
	2	130.39	296.34	18.26
Q345R	1	175.97	399.93	11.64
	2	168.00	381.82	13.10
18MnMoNbR	1	231.00	525.00	17.46
	2	250.27	568.80	17.82

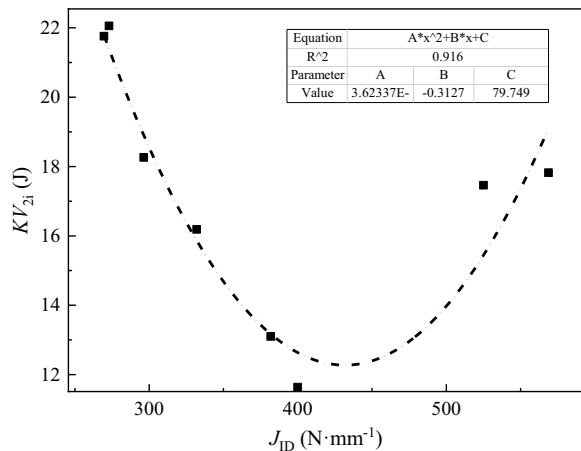


Figure 32 KV_{2i}-J_{ID} plot from tests and the fitting curve

the Charpy impact test. The KV_{2i}-J_{ID} plot and fitting curve are shown in Figure 32. The crack initiation energy KV_{2i} can be calculated using the fitting formula shown in Eq. (23):

$$KV_{2i} = 0.00036J_{ID}^2 - 0.3127J_{ID} + 79.749. \quad (23)$$

In combination with Eq. (22), the impact absorbed energy KV₂ of a material can be obtained. The value of η is discussed in Section 6.

6 Results and Discussion

6.1 Fracture Toughness by Modified CIE Model

According to the SITs mentioned in Section 2.3, the effective Young’s modulus was calculated using the modified formula in Eq. (16), and the Pharr-Oliver formula in Eq. (15) (i.e., E_{eff} and E_{PO}), and the E_{PO} and E_{eff} from the 1st indentation cycle were assumed to be the E of the undamaged material. Comparisons of E_{PO} and E_{eff} from the 1st indentation cycle with those from the tensile test (E_T) are presented in Table 4. From the comparison, it was found that the error between E_{PO} and E_T is up to 30%. However, the error between E_{eff} and E_T is less than

Table 4 Comparison of E_{PO} and E_{eff} from the 1st indentation cycle

Material	E _T (GPa)	E _{PO} (GPa)	$\frac{E_{PO}-E_T}{E_T}$ (%)	E _{eff} (GPa)	$\frac{E_{eff}-E_T}{E_T}$ (%)
Q345R	190	118	-37.9	180	-5.2
SA508-3	206	144	-30.1	199	-3.4
18Mn	195	132	-32.3	200	2.6
S30408	173	127	26.5	182	5.2

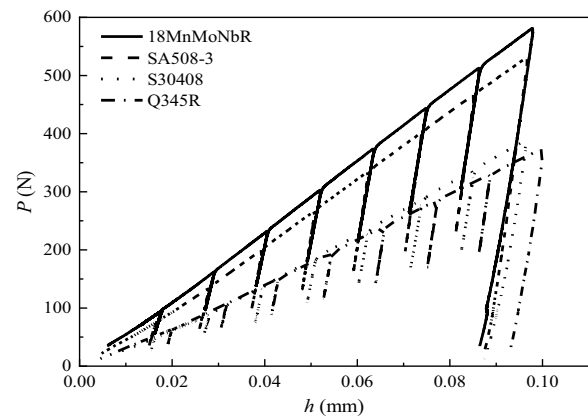


Figure 33 Load-displacement curve obtained from SITs

6%, which proves the validity of the modified effective Young’s modulus model.

The load-displacement curves obtained from the spherical indentation tests are shown in Figure 33. The loading curve is approximately a straight line, which is the result of a superposition of the two nonlinear behaviors in the SITs. One of these is the nonlinearity of the load–displacement curve caused by the geometric nonlinearity of the spherical indenter, and the other is the nonlinearity of the work hardening of the materials. Combined with the load-displacement curve shown in Figure 33, the fracture toughness was calculated using the previous CIE model and the modified CIE model (i.e., K_{ICP} and K_{ICM}, as calculated from Figure 25). A comparison of K_{ICP} and K_{ICM}, with the average results of the mode I fracture test (K_{ICT}) in Section 2.5 is shown in Table 5.

By comparison, it was found that the fracture toughness calculated using the previous CIE model was higher than that of the mode I fracture test. The minimum error of the previous model was more than 20%, and the error for S30408 was up to 51.82%. The larger error is mainly because the effective Young’s modulus obtained in the previous CIE model is not sufficiently accurate [35]. Additionally, the value of the critical damage variable from the previous model was larger (illustrated in Section 4.3), which also led to a large error in the fracture toughness. Compared with the previous CIE model, the modified CIE model result was closer to the experimental results. Except for the error between K_{ICM} and K_{ICT} for 18MnMoNbR, which is approximately 15%, that of other materials is approximately 5%. In addition, the fracture toughness calculated by the modified CIE model is conservative, which is desirable in engineering applications.

Table 5 Comparison of K_{ICP} and K_{ICM} with K_{ICT}

Material	No.	Mode I fracture test K_{ICT} (MPa·m ^{0.5})	Previous CIE model			Modified CIE model		
			h_c (mm)	K_{ICP} (MPa·m ^{0.5})	$\frac{K_{ICP}-K_{ICT}}{K_{ICT}}$ (%)	h_c (mm)	K_{ICM} (MPa·m ^{0.5})	$\frac{K_{ICM}-K_{ICT}}{K_{ICT}}$ (%)
S30408	1	152.33	0.097	183.41	20.40	0.063	144.27	5.29
	2		0.151	231.27	51.82	0.064	147.80	-2.97
SA508-3	1	171.13	0.098	231.14	35.07	0.057	175.9	2.78
	2		0.101	235.45	37.58	0.051	165.18	-3.47
Q345R	1	176.70	0.202	248.73	40.76	0.091	165.7	-6.23
	2		0.207	261.87	48.20	0.095	167.7	-5.09
18MnMoNbR	1	223.00	0.158	296.32	32.87	0.071	192.78	-13.55
	2		0.178	317.52	42.38	0.064	184.37	-17.32

Table 6 Comparison of KV_2 with KV_{2i}

Material	No.	KV_{2i} (J)	KV_2 (J)	$\frac{KV_{2i}-KV_2}{KV_2}(\eta_i)$ (%)
S30408	1	21.75757	307	7.09
	2	22.05407	314	7.02
SA508-3	1	16.18597	193	8.34
	2	18.26295	184.5	9.90
Q345R	1	11.63808	193	6.03
	2	13.09879	191	6.86
18MnMoNbR	1	17.4609	237	7.37
	2	17.82138	227	7.85

6.2 Impact Absorbed Energy by Modified CIE Model

The impact absorbed energy, KV_2 and crack initiation energy KV_{2i} of the four materials were calculated based on the Charpy impact tests, as shown in Table 6.

It is important to note that the range of η_i shown in Table 6 is relatively concentrated, with a minimum value of 6.03% and a maximum value of 9.9%. To avoid over-estimating the material performance in engineering applications, the maximum η_i ($\eta=9.9\%$) was also used

to calculate the impact absorption energy. A comparison between KV_{2S} as calculated from SITs and KV_2 obtained from the impact tests is shown in Table 7.

When η was 9.9%, the maximum error between the impact absorbed energy determined by the SITs and that from the Charpy impact test was 45.42%. However, only two sets of data are larger than 30%, and both are lower than the experimental values, indicating that the results are in accordance with the safety requirements for engineering applications. When the impact absorbed energy was calculated from SITs using the material’s own crack initiation energy ratio (i.e., $\eta=\eta_i$), the minimum error was 4.44%, the maximum was 27.4%, and there are six sets of data with an error of less than 21%. From the results, it can be concluded that it is feasible to estimate the impact absorbed energy using spherical indentation tests; however, the calculation accuracy still needs to be discussed. The usability of this method can be further improved after the establishment of a comprehensive database.

Table 7 Comparison between the calculated value KV_{2S} and the experimental value KV_2

Material	No.	KV_2 (J)	J_{ID} (N/mm)	KV_{2i} (J)	$(\eta=\eta_i)$		$(\eta=9.9\%)$	
					KV_{2S} (J)	$\frac{KV_{2S}-KV_2}{KV_2}(\%)$	KV_{2S} (J)	$\frac{KV_{2S}-KV_2}{KV_2}(\%)$
S30408	1	307	260.48	22.72	320.62	4.44	231.87	-24.47
	2	314	248.18	24.31	346.21	10.26	248.13	-20.98
SA508-3	1	193	310.64	17.35	206.89	7.20	177.05	-8.266
	2	184.5	273.94	21.10	213.19	15.55	215.34	16.71
Q345R	1	193	344.34	14.76	244.75	26.81	150.60	-21.97
	2	191	336.18	15.31	223.29	16.89	156.24	-18.20
18MnMoNbR	1	237	386.26	12.68	172.06	-27.40	129.35	-45.42
	2	227	353.29	14.21	180.98	-20.27	144.98	-36.13

7 Conclusions

To address the problem of conventional approaches for mechanical property determination requiring destructive sampling, which may be unsuitable for in-service structures, a method for determining the quasi-static fracture toughness and impact absorbed energy from SITs is proposed in this study. The stress status and damage mechanism of specimens under SITs, mode I fracture tests, and Charpy impact tests were first investigated using FE calculations and SEM observations. Subsequently, the widely used CIE model for quasi-static fracture toughness determination from the SITs was modified. The quasi-static fracture toughness, as determined by the CIE model, was employed for the assessment of impact absorbed energy, in conjunction with dynamic fracture toughness and crack initiation energy. The effectiveness of the newly proposed method was verified through experiments on four types of steel: Q345R, SA508-3, 18MnMoNbR, and S30408. The following conclusions were drawn from the investigations mentioned above.

- (1) The damage in the mode I fracture originates from void nucleation, growth, and coalescence in the high stress triaxiality region, which is similar to the results from uniaxial tensile tests. However, the indentation damage originates from a dislocation pile-up in a low stress triaxiality region, which is similar to that from pure shear tests. Therefore, the SIT and mode I fractures can be correlated by determining the relationship between the uniaxial tensile and pure shear tests.
- (2) From cyclic-loading tensile tests on the four metal materials, it was found that the critical tensile damage variable varied between 0.20 and 0.23 (conservatively set to 0.2). Correspondingly, the critical shear damage variable, which is applicable to SITs, was 0.25.
- (3) Compared with the previous CIE model, the modified CIE model considers the damage mechanism and is more effective in the quasi-static fracture toughness calculation (with the maximum error decreasing from 51.82% to 17.32%).
- (4) When the impact absorbed energy is calculated from the SITs using the material's own crack initiation energy ratio (i.e., $\eta = \eta_i$), the maximum error is approximately 25%. Enhanced calculation accuracy can be achieved upon the development of a more comprehensive database for crack-initiation energy ratios. In this case, SIT can be considered as an alternative method for evaluating the impact of absorbed energy.

Acknowledgements

The authors sincerely thank the China Scholarship Council and Shandong University Testing and Manufacturing Center for Advanced Materials for their assistance.

Authors' Contributions

TZ and WW were in charge of the entire trial; JL wrote the manuscript; SW and JC assisted with the sampling and laboratory analysis. All authors have read and approved the final manuscript.

Authors' Information

Jianxun Li born in 1993, is currently a PhD candidate at *School of Mechanical Engineering, Shandong University, China*. He received his graduate degree from *Chinese University of Petroleum, China*, in 2019. His research interests include nondestructive testing and ultrahigh cycle fatigue.

Tairui Zhang born in 1991, received his PhD degree from *School of Mechanical Engineering, Shandong University, China*, 2018, and is currently a staff member at *School of Mechanical Engineering, Southeast University, China*. His research interests include materials testing and mechanics.

Shang Wang born in 1994, received his master's degree from *School of Mechanical Engineering, Shandong University, China*, in 2018. Her main research areas include engineering failure analysis and determination of fracture toughness.

Jirui Cheng born in 1994, received his master's degree from *School of Mechanical Engineering, Shandong University, China*, in 2019.

Weiqiang Wang born in 1959, received his PhD degree from *School of Mechanical and Power Engineering, East China University of Science and Technology, China*, in 1990. He is currently a professor at *School of Mechanical Engineering Shandong University, China*. His research interests include engineering failure analysis, supercritical fluid technology and material testing.

Funding

Supported by National Natural Science Foundation of China (Grant No. 52275154), and National Key Research and Development Project of China (Grant No. 2016YFF0203005).

Availability of Data and Materials

All data generated or analyzed during this study are included in this published article (and its additional files).

Declarations

Competing Interests

The authors declare no competing financial interests.

Received: 21 January 2021 Revised: 26 July 2022 Accepted: 10 July 2023
Published online: 20 September 2023

References

- [1] T Zhang, S Wang, W Wang. An energy-based method for flow property determination from a single-cycle spherical indentation test (SIT). *International Journal of Mechanical Sciences*, 2020, 171.
- [2] H Chen, L X Cai. An elastoplastic energy model for predicting the deformation behaviors of various structural components. *Applied Mathematical Modelling*, 2019, 68: 405–421.
- [3] F Yu, P Y Ben Jar, M T Hendry. Indentation for fracture toughness estimation of high-strength rail steels based on a stress triaxiality-dependent ductile damage model. *Theoretical and Applied Fracture Mechanics*, 2018, 94: 10–25.
- [4] S Wu, T Xu, M Song, et al. Mechanical properties characterisation of welded joint of austenitic stainless steel using instrumented indentation technique. *Materials at High Temperatures*, 2016, 33(3): 270–275.
- [5] S Ghosh, R V Prakash. Study of damage and fracture toughness due to influence of creep and fatigue of commercially pure copper by monotonic and cyclic indentation. *Metallurgical and Materials*

- Transactions a-Physical Metallurgy and Materials Science*, 2013, 44A(1): 224–234.
- [6] T S Byun, J W Kim, J H Hong. A theoretical model for determination of fracture toughness of reactor pressure vessel steels in the transition region from automated ball indentation test. *Journal of Nuclear Materials*, 1998, 252(3): 187–194.
- [7] T L Anderson. *Fracture mechanics*. Taylor and Francis, 2017.
- [8] F M Haggag, T S Byun, J H Hong, et al. Indentation-Energy-to-Fracture (IEF) parameter for characterization of DBTT in carbon steels using nondestructive Automated Ball Indentation (ABI) technique. *Scripta Materialia*, 1998, 38(4): 645–651.
- [9] G X Zhang, S Wang, W Q Wang. Research on the evaluation of Q345R steel fracture toughness by automated indentation testing method. *Mechatronics*, 2017, 23(06): 23–29. (in Chinese)
- [10] J S Lee, J Jang, B W Lee, et al. An instrumented indentation technique for estimating fracture toughness of ductile materials: A critical indentation energy model based on continuum damage mechanics. *Acta Materialia*, 2006, 54(4): 1101–1109.
- [11] J Li, F Li, X Ma, et al. A strain-dependent ductile damage model and its application in the derivation of fracture toughness by micro-indentation. *Materials & Design*, 2015, 67: 623–630.
- [12] S Ghosh, G Das. Effect of pre-strain on the indentation fracture toughness of high strength low alloy steel by means of continuum damage mechanics. *Engineering Fracture Mechanics*, 2012, 79: 126–137.
- [13] N Han, X Zhang, S Liu, et al. Effects of pre-stretching and ageing on the strength and fracture toughness of aluminum alloy 7050. *Materials Science and Engineering a-Structural Materials Properties Microstructure and Processing*, 2011, 528(10-11): 3714–3721.
- [14] H Andersson. Analysis of a model for void growth and coalescence ahead of a moving crack tip. *Journal of the Mechanics and Physics of Solids*, 1977, 25(3): 217–233.
- [15] Y B Bao, T Wierzbicki. A comparative study on various ductile crack formation criteria. *Journal of Engineering Materials and Technology-Transactions of the ASME*, 2004, 126(3): 314–324.
- [16] J H Pan. *Dynamic fracture behavior of pressure vessel metal materials under impact loads*. Anhui: University of Science and Technology of China, 2013. (in Chinese)
- [17] J M Barsom, S T Rolfe. Correlations between $K_{sub} I_c$ and Charpy V-notch test results in the transition-temperature range. *Impact Testing of Metals*, 1970, 3: 281–302.
- [18] P Hübner, G Pusch. Correlations between Charpy energy and crack initiation parameters of the J-integral-concept. *European Structural Integrity Society*, 2002, 30(02): 289–295.
- [19] R J Smith, A J Horn, A H Sherry. Relating Charpy energy to fracture toughness in the lower transition region using a Weibull stress dependent energy scaling model. *International Journal of Pressure Vessels and Piping*, 2018, 166: 72–83.
- [20] T Zhang, S Wang, W Wang. A comparative study on fracture toughness calculation models in spherical indentation tests (SITs) for ductile metals. *International Journal of Mechanical Sciences*, 2019, 160: 114–128.
- [21] T Zhang, S Wang, W Wang. A unified energy release rate based model to determine the fracture toughness of ductile metals from unnotched specimens. *International Journal of Mechanical Sciences*, 2019, 150: 35–50.
- [22] M Z Shi, Z Q Huang, R K Lu. Study of the relation between the simple tension damage factor $D1c$ and pure shear damage factor. *Journal of Zhejiang University (Natural Science)*, 1988(06): 25–29. (in Chinese)
- [23] General Administration of Quality Supervision, Inspection and Quarantine of the People's Republic of China; Standardization Administration of the People's Republic of China. GB/T 13-2014, Steel plates for boilers and pressure vessels. Beijing: China Standard Publishing House, 2014. (in Chinese)
- [24] ASTM A508 / A508M-17, Standard specification for quenched and tempered vacuum-treated carbon and alloy steel forgings for pressure vessels. ASTM International, West Conshohocken, PA, USA, 2017. <http://www.astm.org>.
- [25] General Administration of Quality Supervision, Inspection and Quarantine of the People's Republic of China; Standardization Administration of the People's Republic of China. GB/T 12771–2019, Welded stainless steel pipes for liquid delivery. Beijing: China Standard Publishing House, 2019. (in Chinese)
- [26] General Administration of Quality Supervision, Inspection and Quarantine of the People's Republic of China; Standardization Administration of the People's Republic of China. GB/T 228.1–2010, Metallic materials-tensile testing part 1: method of test at room temperature. Beijing: China Standard Publishing House, 2007. (in Chinese)
- [27] General Administration of Quality Supervision, Inspection and Quarantine of the People's Republic of China; Standardization Administration of the People's Republic of China. GB/T 21143–2014, Metallic materials-unified method of test for determination of quasistatic fracture toughness. Beijing: China Standard Publishing House, 2014. (in Chinese)
- [28] General Administration of Quality Supervision, Inspection and Quarantine of the People's Republic of China; Standardization Administration of the People's Republic of China. GB/T 229–2007, Metallic materials—Charpy pendulum impact test method. Beijing: China Standard Publishing House, 2007. (in Chinese)
- [29] R Chaouadi, J L Puzolante. Loading rate effect on ductile crack resistance of steels using precracked Charpy specimens. *International Journal of Pressure Vessels and Piping*, 2008, 85(11): 752–761.
- [30] T Zhang, S Wang, W Wang. Improved methods to determine the elastic modulus and area reduction rate in spherical indentation tests. *Materials Testing*, 2018, 60(4): 355–362.
- [31] R Johnson, W K Cook. A constitutive model and data for metals subjected to large strains high strain rates and high temperatures. *Seventh International Symposium on Ballistics*, 1983: 541–548.
- [32] Y B Bao, T Wierzbicki. On fracture locus in the equivalent strain and stress triaxiality space. *International Journal of Mechanical Sciences*, 2004, 46(1): 81–98.
- [33] C Zener. *Fracturing of metals*. Cleveland OH: American Society of Metals, 1948.
- [34] J Lemaitre. A continuous damage mechanics model for ductile fracture. *Journal of Engineering Materials and Technology-Transactions of the ASME*, 1985, 107(1): 83–89.
- [35] N Bonora. A nonlinear CDM model for ductile failure. *Engineering Fracture Mechanics*, 1997, 58(1-2): 11–28.
- [36] T Sritharan, R S Chandel. Phenomena in interrupted tensile tests of heat treated aluminium alloy 6061. *Acta Materialia*, 1997, 45(8): 3155–3161.
- [37] W C Oliver, G M Pharr. Measurement of hardness and elastic modulus by instrumented indentation: Advances in understanding and refinements to methodology. *Journal of Materials Research*, 2004, 19(1): 3–20.
- [38] W C Oliver, G M Pharr. An improved technique for determining hardness and elastic-modulus using load and displacement sensing indentation experiments. *Journal of Materials Research*, 1992, 7(6): 1564–1583.
- [39] R Chaouadi. An energy-based crack extension formulation for crack resistance characterization of ductile materials. *Journal of Testing and Evaluation*, 2004, 32(6): 469–475.
- [40] R Tomasek, V Mares, L Horsak. Fracture toughness and Charpy impact test of MIM steels and correlation of results by KIC- CVN relationships. *Key Engineering Materials*, 2019, 810: 1–6.
- [41] H F Li, Q Q Duan, P Zhang, et al. The quantitative relationship between fracture toughness and impact toughness in high-strength steels. *Engineering Fracture Mechanics*, 2019, 211: 362–370.

Submit your manuscript to a SpringerOpen[®] journal and benefit from:

- Convenient online submission
- Rigorous peer review
- Open access: articles freely available online
- High visibility within the field
- Retaining the copyright to your article

Submit your next manuscript at ► springeropen.com